Climate response to negative greenhouse gas radiative forcing in polar winter

M. G. Flanner[1], X. Huang[1], X. Chen[1], and G. Krinner[2]

[1]Department of Climate and Space Sciences and Engineering, University of Michigan, Ann Arbor, Michigan, USA.

[2]CNRS, Univ. Grenoble Alpes, Institut des Géosciences de l'Environnement (IGE), 38000 Grenoble, France

Key Points:

- Increased GHG concentrations in polar inversion layers cause negative top-of-atmosphere instantaneous and effective radiative forcing
- Polar and global surface temperatures warm despite this negative radiative forcing
- Surface warming and tropospheric cooling result from high stability and increased surface downwelling longwave flux

This is the author manuscript accepted for publication and has undergone full peer review but has not been through the copyediting, typesetting, pagination and proofreading process, which may lead to differences between this version and the Version of Record. Please cite this article as doi: 10.1002/2017GL076668

Corresponding author: Mark Flanner, flanner@umich.edu

Abstract

Greenhouse gas (GHG) additions to Earth's atmosphere initially reduce global outgoing longwave radiation (OLR), thereby warming the planet. In select environments with temperature inversions, however, increased GHG concentrations can actually increase local OLR. Negative top-of-atmosphere and effective radiative forcing (ERF) from this situation give the impression that local surface temperatures could cool in response to GHG increases. Here we consider an extreme scenario in which GHG concentrations are increased only within the warmest layers of winter near-surface inversions of the Arctic and Antarctic. We find, using a fully coupled Earth system model, that the underlying surface warms despite the GHG addition exerting negative ERF and cooling the troposphere in the vicinity of the GHG increase. This unique radiative forcing and thermal response is facilitated by the high stability of the polar winter atmosphere, which inhibits thermal mixing and amplifies the impact of surface radiative forcing on surface temperature. These findings also suggest that strategies to exploit negative ERF via injections of short-lived GHGs into inversion layers would likely be unsuccessful in cooling the planetary surface.

1 Introduction

Increasing concentrations of greenhouse gases (GHGs) warm Earth by causing an immediate reduction in the flux of outgoing longwave radiation (OLR) from the planet to space [e.g., *Arrenhius*, 1896]. OLR decreases because the atmosphere is generally colder than the underlying surface, and atmospheric emissivity increases with elevated GHG amounts. In atmospheric environments with temperature inversions (i.e., where temperature increases with height), however, increased GHG concentrations can actually increase OLR by raising the emissivity of a relatively warm portion of the surface–atmosphere column [e.g., *Schmithüsen et al.*, 2015; *Huang et al.*, 2016; *Sejas et al.*, 2016]. This effect can be demonstrated analytically if we neglect scattering, in which case top-of-atmosphere (TOA) outgoing nadir-view radiance from an absorbing atmosphere is [e.g., *Thomas and Stamnes*, 1999]:

$$I_\lambda^\uparrow(\infty) = B_\lambda[T_s]\,\mathcal{T}_\lambda^* + \int_0^\infty B_\lambda[T(z)]\,\frac{\partial \mathcal{T}_\lambda(z,\infty)}{\partial z}\,dz \tag{1}$$

Here, B_λ is Planck's function evaluated at temperature T and wavelength λ, T_s is the blackbody surface temperature, $\mathcal{T}_\lambda^*$ is the whole-atmosphere transmittance, $\mathcal{T}_\lambda(z,\infty)$ is the transmittance between z and the TOA, and subscript λ indicates wavelength-dependent quantities. With a GHG that has vertical density profile $\rho(z)$ and mass absorption cross-section k_λ, the transmittance function is $\mathcal{T}_\lambda(z,\infty) = \exp[-k_\lambda \int_z^\infty \rho(z)\,dz]$. Assuming idealized and carefully chosen gas and temperature profiles depicted in Figure 1, we see that the peak of the weighting function ($\partial\mathcal{T}_\lambda/\partial z$) shifts to a higher and colder location of the atmosphere with elevated GHG under normal atmospheric conditions, but shifts to a higher and *warmer* location under the temperature inversion scenario, in this case producing an instantaneous increase in upwelling radiance at the model top.

Regions of Earth's atmosphere with persistent temperature inversions include the stratosphere and winter lower troposphere of polar regions [e.g., *Phillpot and Zillman*, 1970; *Serreze et al.*, 1992; *Connolley*, 1996]. Hence, negative TOA radiative forcing can result from increased GHG concentrations occurring in isolation in these regions, as seen from the water vapor radiative kernels depicted in Figure 2 of *Soden et al.* [2008] and Figure 1 of *Shell et al.* [2008]. *Schmithüsen et al.* [2015] and *Huang et al.* [2016] showed that increased CO_2 throughout the atmospheric column can produce negative TOA forcing over central Antarctica, where the stratosphere (and origin of OLR near the center of the 15μm CO_2 absorption band) is often warmer than the surface. Similarly, smaller surface–

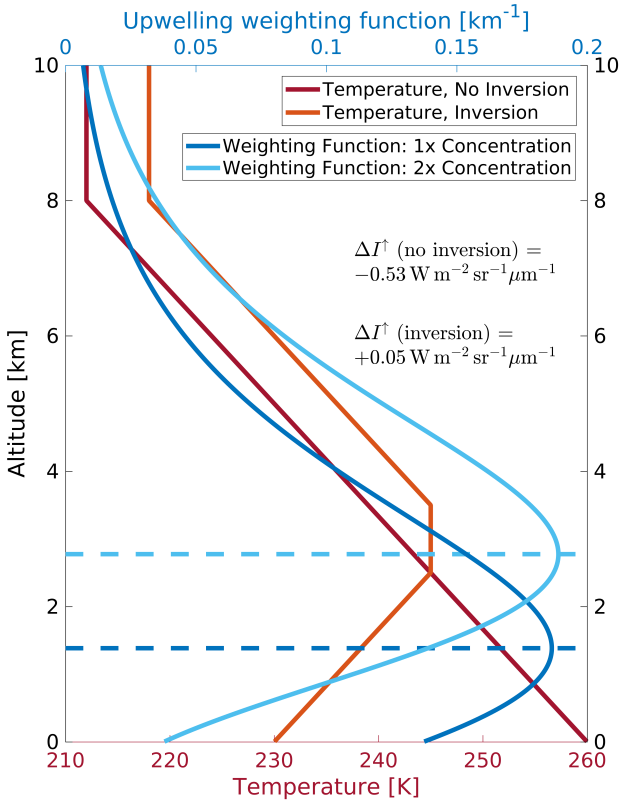

Figure 1. Red curves: Idealized temperature profiles without and with a near-surface temperature inversion. Blue curves: Weighting functions ($\partial\mathcal{T}/\partial z$) for 11 µm outgoing nadir-view intensity ($I^{\uparrow}$) in columns with a hypothetical greenhouse gas that has a mass absorption cross-section of 1.0 $\mathrm{m^2\,kg^{-1}}$, scale height of 2 km, and surface densities of 1.0 and 2.0 $\mathrm{g\,m^{-3}}$, respectively, in the 1× and 2× concentration scenarios. Dotted horizontal lines show the altitudes where the weighting functions peak. With additional greenhouse gas, $I^{\uparrow}$ at the model top (Equation 1) decreases when there is no temperature inversion but increases when there is an inversion.

atmosphere temperature contrast in polar regions leads to weaker annual-mean longwave forcing from increased CO_2 [*Myhre and Stordal*, 1997; *Shine and Forster*, 1999; *Hansen et al.*, 2005] and tropospheric ozone [*Stevenson et al.*, 2013]. Early studies of nuclear winter also noted that the global greenhouse effect becomes inhibited when the upper troposphere and lower stratosphere experience extreme warming [*Turco et al.*, 1983].

Under both non-inversion and inversion scenarios, however, downwelling longwave flux at the surface increases with elevated GHGs, despite the opposite sign of TOA radiative perturbation that can occur in these two scenarios. This leads us to the question:

How does the climate system respond to GHG increases occurring in tropospheric temperature inversion environments? Judging only from the TOA or tropopause forcing, one might expect surface cooling. Indeed, in the context of near-zero TOA forcing over central Antarctica from increased CO_2, *Schmithüsen et al.* [2015] note that this region has not warmed in recent decades. If surface cooling is expected, this even raises the possibility that injections of short-lived GHGs into polar inversion layers could cool the planetary surface. We show here that although the troposphere cools in response to such radiative forcing, which is negative in both the instantaneous and effective forcing contexts defined by the Intergovernmental Panel on Climate Change (IPCC) [*Myhre et al.*, 2013], the local surface warms.

2 Methods

To explore the effects of increased GHG amounts within polar near-surface inversion layers we conduct model simulations with sharply elevated concentrations of CFC-11 (CCl_3F). This agent is used for convenience because it is a potent greenhouse gas, but the type of gas assumed here is relatively unimportant because our fundamental question pertains simply to how surface and atmospheric temperatures respond to a negative radiative forcing caused by increased emissivity of a tropospheric inversion layer.

First, to illustrate the effect of our designed perturbation with a detailed radiative transfer solution, we apply high spectral resolution ($1\,cm^{-1}$) calculations from the MODerate resolution atmospheric TRANsmission Model 5 (MODTRAN) [e.g., *Berk et al.*, 2014]. We apply typical clear-sky polar winter vertical profiles of temperature, specific humidity, and ozone from ERA-Interim reanalysis [*Dee et al.*, 2011]. The Antarctic profile is an average over the high plateau (elevations over 2 km) from July 2008, identical to the profile applied by *Chen et al.* [2014], and the Arctic profile represents an average over $66 - 90\,^{\circ}N$ during January 2008. Both profiles exhibit a strong near-surface inversion. We set CFC-11 concentrations to zero in baseline simulations and specify a burden of $7.3\,g\,m^{-2}$ (0.12 atm cm) within the tropospheric layer of maximum temperature in perturbed simulations. This value matches that specified in global simulations described next, and was chosen to achieve radiative forcings of order $1\,W\,m^{-2}$.

We conduct two simulations (control and experiment) with the Community Earth System Model (CESM) version 1.0.6 [e.g., *Hurrell et al.*, 2013], configured with fully

coupled atmosphere, ocean, and land model components (component set "B_1850" with horizontal resolution of $1.9 \times 2.5°$). Both simulations start in 1850 from identical equilibrium climate states and have annually-repeating boundary conditions, including prescribed 1850 concentrations of carbon dioxide, methane, nitrous oxide, and ozone. As with the MODTRAN simulations, all CFC concentrations are zero in the control simulation, and in the idealized experiment we apply a CFC-11 mass mixing ratio of 10 ppm within a single atmospheric layer (the 4th from bottom, spanning roughly 770 – 1365 m above the surface), uniformly over 66 – 90 °N during the months of December through February, and uniformly over 66 – 90 °S during the months of June through August. These polar winter environments exhibit persistent near-surface inversions. In the control simulation, peak tropospheric temperatures occur, on average, in the layer where we apply CFC-11 (Figure 2). However, temperatures peak nearer to the ground over high elevation areas of Antarctica (Figure 2) and Greenland (not shown), and hence the radiative impact of this perturbation is somewhat reduced in these regions. The atmosphere component of CESM adopts a terrain-following hybrid-sigma pressure coordinate system, so the altitude above surface of the forcing layer is rather consistent, with standard deviation of 40 m over all perturbed gridcells. Although this experiment is unrealistic because it prohibits gas diffusion and mixing outside of the specified forcing layer, it serves as a boundary case for evaluating the impact of elevated GHG amounts in tropospheric inversion layers. We compare climatological mean states of the final 20 years of 100-year control and experiment simulations. Linearly regressed trends in surface temperature and net TOA radiative flux in the control run were not significant. We calculate the direct instantaneous radiative forcing (IRF) of CFC-11 at the TOA, 200 hPa, and surface by differencing radiative transfer calculations conducted each time-step with and without the CFC-11 perturbation.

We conduct a second pair of CESM simulations to diagnose effective radiative forcing (ERF) [*Hansen et al.*, 2005]. ERF is calculated with fixed sea-surface temperatures (SSTs) but allowing for all rapid adjustments to the atmosphere. ERF was adopted by the IPCC Assessment Report 5 and is suggested to be a better proxy of eventual surface temperature change, but has the disadvantage of being noisier than IRF and requiring longer model integration [*Myhre et al.*, 2013; *Forster et al.*, 2016]. Following techniques described by *Forster et al.* [2016], we conduct two 50-year atmosphere simulations with fixed annually-repeating SSTs and sea-ice distributions representative of 1850 (component set "F_1850"), with and without the 10 ppm CFC-11 perturbation. We derive ERF as the

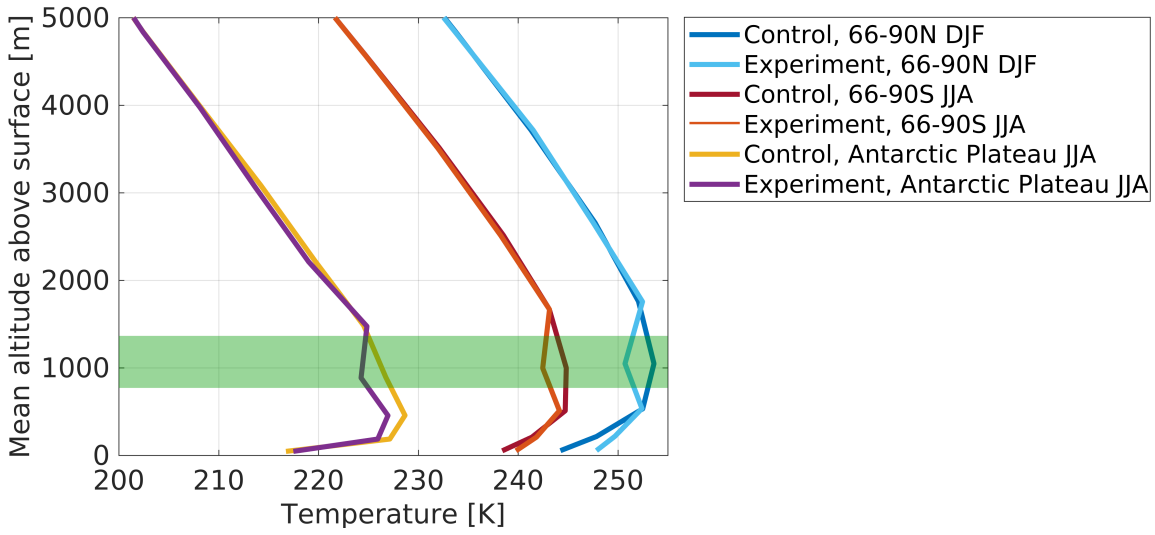

Figure 2. Vertical profiles of temperature from CESM simulations, averaged over the Arctic (66–90°N) during December–February, the Antarctic (66–90°S) during June–August, and a portion of the East Antarctic Plateau (80–85°S, 54–86°E) during June–August. The control simulation has no CFC-11 whereas the experiment applies a mass mixing ratio of 10 ppm in the model layer with mean extent shown in green shading.

difference in net TOA radiative energy flux between these runs, with confidence intervals determined from interannual variations.

3 Results and Discussion

In general, longwave radiative perturbations induced by gas or cloud changes occurring at any particular altitude will depend on the vertical distributions of temperature and molecules that absorb in the same spectral region as the perturbed agent [e.g., *Stephens et al.*, 2012]. Single column MODTRAN simulations of clear-sky TOA and surface spectral fluxes for the situation explored here are shown in Figure 3. It is evident that the perturbation increases both OLR and surface downwelling irradiance, primarily via the strong CFC-11 absorption bands near 840 cm^{-1} and 1080 cm^{-1}, which both lie in the water vapor window. Spectrally integrated changes in these fluxes (listed in the figure) are greater in the Arctic than Antarctic at the surface, and greater in the Antarctic at the TOA. These relative effects result from a warmer Arctic troposphere and a stronger Antarctic temperature inversion.

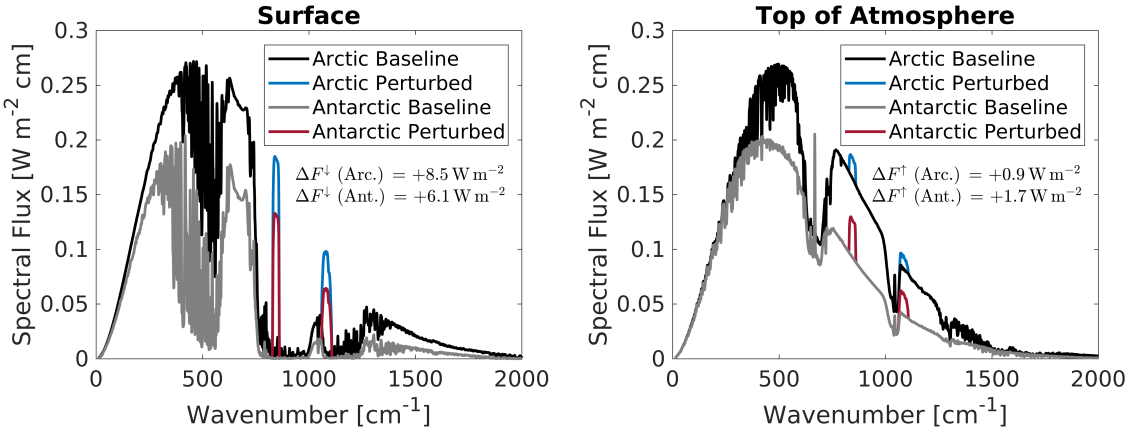

Figure 3. Surface (left) and top-of-atmosphere (right) clear-sky spectral fluxes calculated with MODTRAN using vertical atmospheric profiles from ERA-Interim reanalysis. Arctic profiles are from January 2008 and Antarctic profiles are from July 2008. The perturbed scenarios assume CFC-11 burdens of 7.3 g m^{-2} (0.12 atm cm) in the model layer of maximum tropospheric temperature.

Figure 4 shows the all-sky IRF of the CFC-11 perturbation in the CESM experiment, averaged over December–February (Arctic) and June–August (Antarctic) of the first year of simulation. Consistent with the single-column MODTRAN calculations, we see that the TOA and 200 hPa IRFs are negative while the surface IRF is positive. The winter season TOA and surface IRFs averaged over the Arctic are −0.16 and +1.11 W m^{-2}, respectively, and over the Antarctic they are −0.11 and +0.88 W m^{-2}. Figure 4 shows that the 200 hPa IRF, an approximation of forcing at the tropopause, is nearly identical to the TOA forcing, an unsurprising feature given that the perturbation is introduced in the lower troposphere. The TOA and 200 hPa IRFs are slightly positive in the Norwegian Sea where inversions are absent or weak. Moreover, the IRF is greater over low-elevation areas than over the high plateaus of Antarctica and Greenland. Temperature profiles show that the inversion tends to peak closer to the surface over high elevation areas (Figure 2), slightly beneath the layer of imposed GHG increase. Hence if the perturbation had been introduced lower we would have seen larger forcing over central Antarctica and Greenland, and smaller forcing at lower elevations. We also note that the IRF weakens slightly throughout the simulation, due to Arctic warming and reduced inversion strength, with global annual-mean IRFs of −28, −27, and −25 mW m^{-2} in the first year, years 2–20, and years 81–100, respectively.

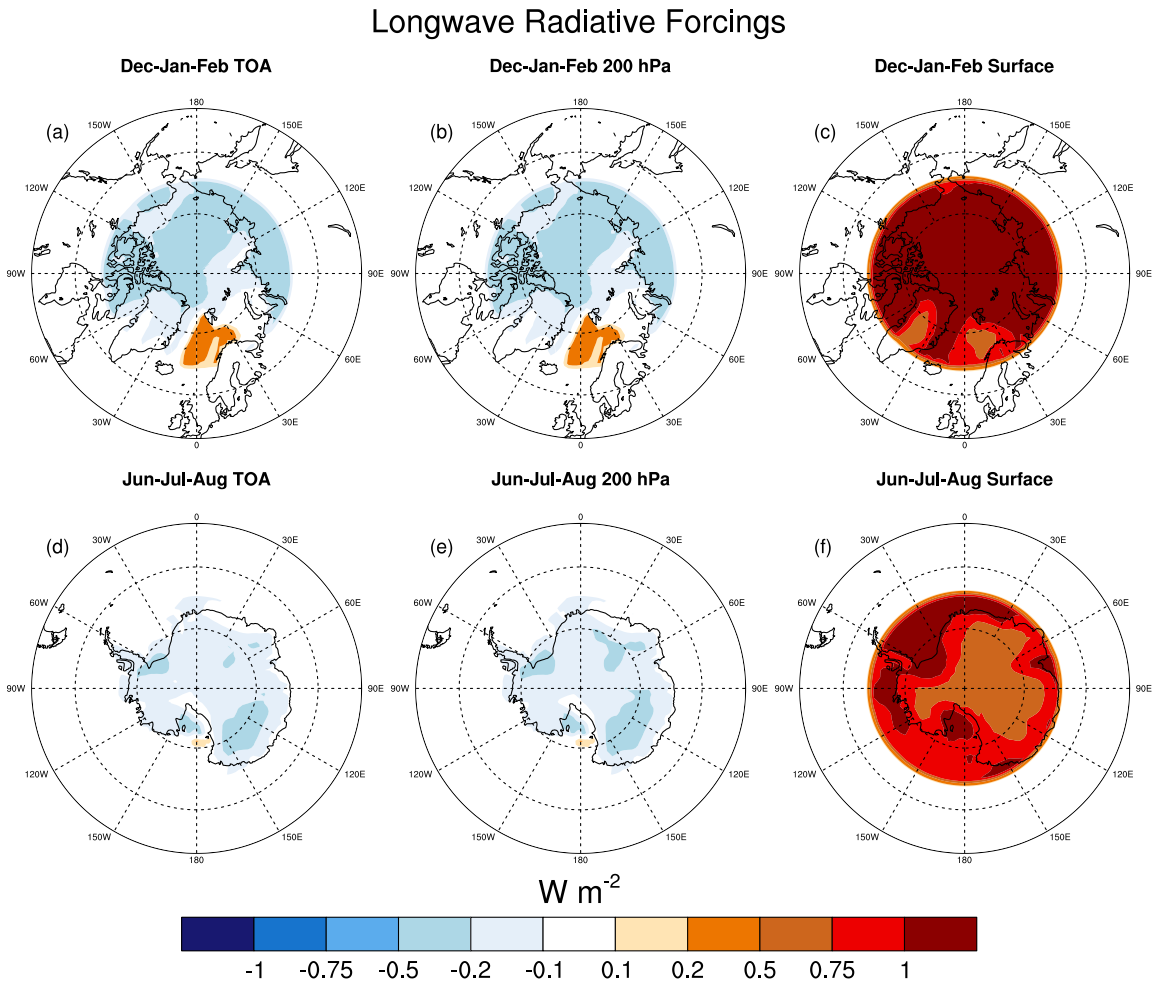

178 **Figure 4.** Instantaneous perturbations to the (a,d) top-of-atmosphere, (b,e) 200 hPa, and (c,f) surface ra-
179 diative energy budgets caused by the addition of CFC-11, averaged over December–February (top row) and
180 June–August (bottom row) in the CESM experiment simulation.

183 Atmospheric temperatures respond to this unique forcing by cooling 2–3°C within
184 the layer of elevated CFC-11 (Figure 2). Cooling of the warmest layer of the inversion
185 is logically expected because emission from this layer increases more than the increase
186 in absorption that also occurs. As can be seen in Figure 5, however, surface tempera-
187 tures warm substantially in the months and regions of active forcing. This warming results
188 from increased surface downwelling longwave flux and occurs despite tropospheric cool-

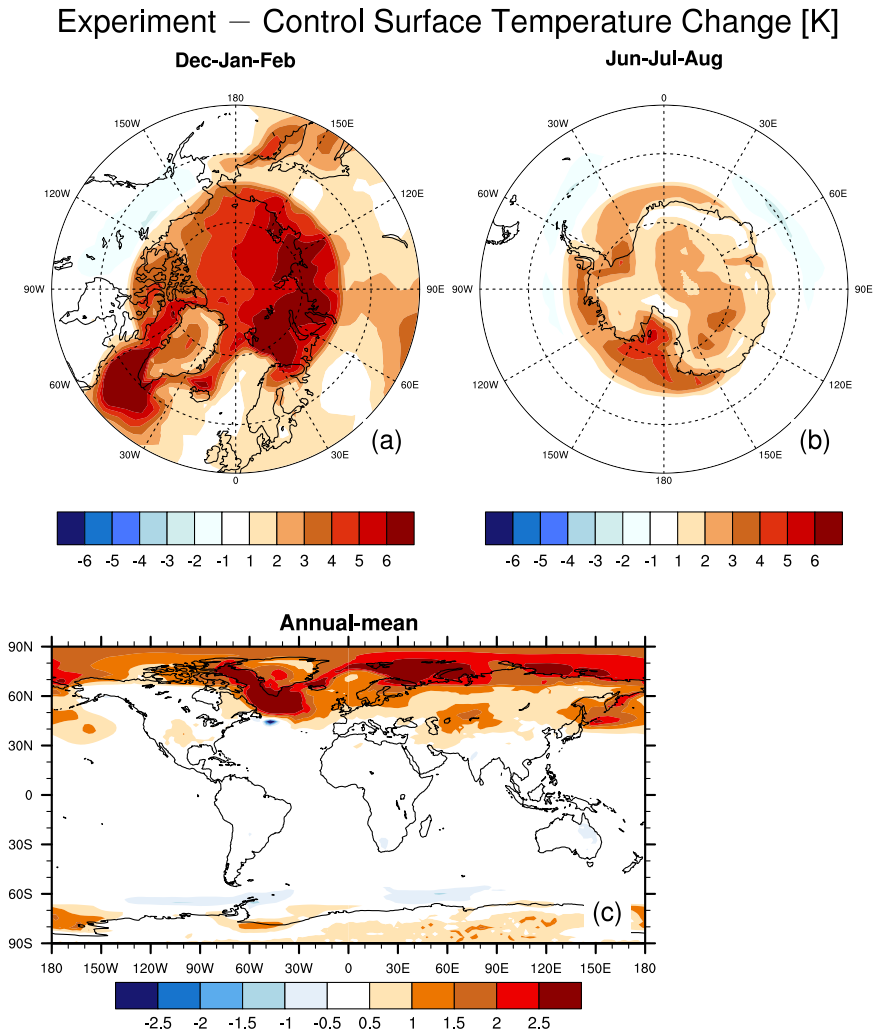

181 **Figure 5.** Differences in surface temperature between the final 20 years of the experiment and control
182 CESM simulations, averaged over (a) December–February, (b) June–August, and (c) the annual-mean.

189 ing caused by negative atmospheric and TOA IRF. The ability for thermal forcings aloft
190 to affect surface temperature depends on the strength of surface–atmosphere coupling and
191 turbulent energy transfer [e.g., *Cess et al.*, 1985; *Ghan et al.*, 1988; *Hansen et al.*, 1997,
192 2005; *Flanner*, 2013]. The polar winter atmosphere is characterized by high stability and
193 near-surface thermal inversions [e.g., *Phillpot and Zillman*, 1970; *Connolley*, 1996; *Serreze*
194 *et al.*, 1992]. Thus, surface perturbations drive larger surface temperature change than in
195 other environments [*Deser et al.*, 2010; *Bintanja et al.*, 2011, 2012; *Pithan and Mauritsen*,

196 2014], in this case enabling the longwave surface forcing to dominate over tropospheric
197 cooling, from which the surface is relatively isolated, and cause net warming of the sur-
198 face. Winter season surface warming in this experiment is 4.5 K in the Arctic and 2.2 K
199 in the Antarctic, and these changes are highly significant ($p < 10^{-10}$) as indicated by t-
200 tests on pooled annual realizations. Arctic surface warming exceeds that in the Antarctic.
201 Moreover, divergence between control and experiment Arctic surface temperatures con-
202 tinues to grow throughout the 100-year simulations, indicating that Arctic feedbacks op-
203 erate to enhance surface warming in the experiment. Indeed, Arctic annual-mean sea-ice
204 coverage decreases by 9.3% in the experiment, serving to amplify near-surface warming.
205 Weaker surface warming over the Antarctic continent is therefore a consequence of both
206 weaker local feedbacks and lower surface forcing, which results from the slight offset be-
207 tween altitudes of gas perturbation and peak temperature described earlier.

208 The global annual-mean surface temperature response in this experiment is +0.2 K
209 (significant at $p < 0.0001$), with weak warming outside of the polar regions (Figure 5c).
210 The ERF diagnosed from fixed-SST runs is $-0.09 \pm 0.07\,\mathrm{W\,m^{-2}}$ in the global mean,
211 $-3.2 \pm 0.9\,\mathrm{W\,m^{-2}}$ in the Arctic during December–February, and $-3.1 \pm 1.0\,\mathrm{W\,m^{-2}}$ over
212 Antarctica during June–August. Thus surface temperatures warm in this experiment de-
213 spite negative ERF and IRF at the TOA and 200 hPa. This therefore represents a rare case
214 where radiative forcing is a poor proxy for surface temperature response. Early studies
215 of nuclear winter also expose unusual relationships between radiative forcing and surface
216 temperature change. *Cess et al.* [1985], in particular, describe the inadequacy of traditional
217 radiative forcing metrics when the surface becomes convectively decoupled from the tro-
218 posphere, a situation not unlike the weak coupling that exists naturally during polar winter.
219 *Thompson et al.* [1987] and *Ghan et al.* [1988] both show that increasing aerosol infrared
220 absorptivity causes the surface to cool less from nuclear explosion-induced smoke, due to
221 the associated increase in downwelling infrared flux at the surface. Although TOA forc-
222 ings associated with this greenhouse-like effect were not reported, they were presumably
223 negative due to the extreme heating that had occurred within the smoke layer. *Hansen*
224 *et al.* [1997] also show that normalized climate response to certain idealized forcings can
225 be "less well behaved", though not to the extremity shown in our experiment. Despite the
226 deficiency of radiative forcing metrics in this unique situation, we note that ERF is a good
227 proxy for climate response to globally-distributed forcings of the type and magnitude that
228 are currently operating [*Hansen et al.*, 1997, 2005; *Myhre et al.*, 2013].

Attribution of surface warming to weak surface–atmosphere coupling in our experiment implies a result whose magnitude is model-dependent, and indeed other studies show that model parameterizations of vertical mixing and atmospheric stability can strongly affect surface temperature response [*Ghan et al.*, 1988; *Bintanja et al.*, 2011, 2012]. With strong surface–atmosphere mixing, however, the temperature inversion would collapse and radiative forcing from the perturbation would consequently become positive. Hence the very situation that permits negative GHG radiative forcing also enables surface warming to occur in spite of the negative forcing. Furthermore, because the temperature response profile acts to weaken the inversion, the IRF becomes less negative with time in the experiment. Finally, we conclude that because greenhouse gas increases do not produce surface cooling in this extreme scenario, in which the gas perturbation is confined to the inversion layer, it is highly unlikely that surface cooling would result from more realistic scenarios that include transport of gas injections. This is because mixing would promote positive ERF to occur in more regions, leading to tropospheric and surface warming happening through the canonical greenhouse forcing mechanism.

4 Conclusions

Motivated by previous work showing that greenhouse gas radiative forcing can be negative in polar regions [*Soden et al.*, 2008; *Shell et al.*, 2008; *Stevenson et al.*, 2013; *Schmithüsen et al.*, 2015; *Huang et al.*, 2016], we conducted an idealized Earth system model experiment to explore the climate impacts of elevated GHG concentrations within polar tropospheric inversion layers. We find that the polar surface warms in response to increased downwelling infrared flux. This occurs despite cooling of the tropospheric layer subjected to increased greenhouse gas and also despite negative instantaneous and effective radiative forcing exerted at the TOA and tropopause. These findings demonstrate that negative radiative forcing associated with GHG additions in extreme polar environments should not be used to infer that local surface cooling will result. More generally, these results illustrate the importance of surface radiative forcing for governing surface temperature response in polar regions, where stable atmospheric conditions, especially during winter, act to decouple the surface from the atmosphere.

Acknowledgments

We thank two anonymous reviewers for providing constructive comments on our manuscript. We acknowledge support from U.S. National Science Foundation grant ARC-1253154 and Department of Energy grant DE-SC0012969. CESM source code can be obtained from: http://www.cesm.ucar.edu/. Model output data can be obtained via the public repository at: https://deepblue.lib.umich.edu/data/concern/generic_works/7h149q43m

References

Arrenhius, S. (1896), On the influence of carbonic acid in the air on the temperature of the ground, *Philos. Mag.*, *41*, 237–276.

Berk, A., P. Conforti, R. Kennett, T. Perkins, F. Hawes, and J. van den Bosch (2014), MODTRAN6: a major upgrade of the MODTRAN radiative transfer code, in *SPIE Defense+ Security*, pp. 90,880H–90,880H, International Society for Optics and Photonics.

Bintanja, R., R. G. Graversen, and W. Hazeleger (2011), Arctic winter warming amplified by the thermal inversion and consequent low infrared cooling to space, *Nature Geosci.*, *4*(11), 758–761, doi:10.1038/ngeo1285.

Bintanja, R., E. C. van der Linden, and W. Hazeleger (2012), Boundary layer stability and Arctic climate change: a feedback study using EC-Earth, *Clim. Dyn.*, *39*(11), 2659–2673, doi:10.1007/s00382-011-1272-1.

Cess, R. D., G. L. Potter, S. J. Ghan, and W. L. Gates (1985), The climatic effects of large injections of atmospheric smoke and dust: A study of climate feedback mechanisms with one- and three-dimensional climate models, *J. Geophys. Res.*, *90*(D7), 12,937–12,950, doi:10.1029/JD090iD07p12937.

Chen, X., X. Huang, and M. G. Flanner (2014), Sensitivity of modeled far-ir radiation budgets in polar continents to treatments of snow surface and ice cloud radiative properties, *Geophys. Res. Lett.*, *41*(18), 6530–6537, doi:10.1002/2014GL061216.

Connolley, W. M. (1996), The Antarctic temperature inversion, *Int. J. Climatol.*, *16*(12), 1333–1342, doi:10.1002/(SICI)1097-0088(199612)16:12<1333::AID-JOC96>3.0.CO;2-6.

Dee, D. P., S. M. Uppala, A. J. Simmons, P. Berrisford, P. Poli, S. Kobayashi, U. Andrae, M. A. Balmaseda, G. Balsamo, P. Bauer, P. Bechtold, A. C. M. Beljaars, L. van de Berg, J. Bidlot, N. Bormann, C. Delsol, R. Dragani, M. Fuentes, A. J. Geer, L. Haimberger, S. B. Healy, H. Hersbach, E. V. Hólm, L. Isaksen, P. Kålberg, M. Köhler, M. Matricardi, A. P. McNally, B. M. Monge-Sanz, J.-J. Morcrette, B.-K. Park, C. Peubey, P. de Rosnay, C. Tavolato, J.-N. Thépaut, and F. Vitart (2011), The ERA-Interim reanalysis: configuration and performance of the data assimilation system, *Q.J.R. Meteorol. Soc.*, *137*(656), 553–597, doi:10.1002/qj.828.

Deser, C., R. Tomas, M. Alexander, and D. Lawrence (2010), The seasonal atmospheric response to projected Arctic sea ice loss in the late twenty-first century, *J. Climate*, *23*(2), 333–351, doi:10.1175/2009JCLI3053.1.

Flanner, M. G. (2013), Arctic climate sensitivity to local black carbon, *J. Geophys. Res. Atmos.*, *118*(4), 1840–1851, doi:10.1002/jgrd.50176.

Forster, P. M., T. Richardson, A. C. Maycock, C. J. Smith, B. H. Samset, G. Myhre, T. Andrews, R. Pincus, and M. Schulz (2016), Recommendations for diagnosing effective radiative forcing from climate models for CMIP6, *J. Geophys. Res. Atmos.*, *121*(20), 12,460–12,475, doi:10.1002/2016JD025320, 2016JD025320.

Ghan, S. J., M. C. MacCracken, and J. J. Walton (1988), Climatic response to large atmospheric smoke injections: Sensitivity studies with a tropospheric general circulation model, *J. Geophys. Res.*, *93*(D7), 8315–8337, doi:10.1029/JD093iD07p08315.

Hansen, J., M. Sato, and R. Ruedy (1997), Radiative forcing and climate response, *J. Geophys. Res.*, *102*, 6831–6864.

Hansen, J., M. Sato, R. Ruedy, L. Nazarenko, A. Lacis, G. A. Schmidt, G. Russell, I. Aleinov, M. Bauer, S. Bauer, N. Bell, B. Cairns, V. Canuto, M. Chandler, Y. Cheng, A. D. Genio, G. Faluvegi, E. Fleming, A. Friend, T. Hall, C. Jackman, M. Kelley, N. Kiang, D. Koch, J. Lean, J. Lerner, K. Lo, S. Menon, R. Miller, P. Minnis, T. Novakov, V. Oinas, J. Perlwitz, J. Perlwitz, D. Rind, A. Romanou, D. Shindell, P. Stone, S. Sun, N. Tausnev, D. Thresher, B. Wielicki, T. Wong, M. Yao, , and S. Zhang (2005), Efficacy of climate forcings, *J. Geophys. Res.*, *110*, D18104, doi:10.1029/2005JD005776.

Huang, Y., X. Tan, and Y. Xia (2016), Inhomogeneous radiative forcing of homogeneous greenhouse gases, *J. Geophys. Res. Atmos.*, *121*(6), 2780–2789, doi:10.1002/2015JD024569, 2015JD024569.

Hurrell, J. W., M. M. Holland, P. R. Gent, S. Ghan, J. E. Kay, P. J. Kushner, J.-F. Lamarque, W. G. Large, D. Lawrence, K. Lindsay, et al. (2013), The Community Earth System Model: A framework for collaborative research, *Bull. Am. Meteor. Soc.*, *94*(9), 1339–1360.

Myhre, G., and F. Stordal (1997), Role of spatial and temporal variations in the computation of radiative forcing and GWP, *J. Geophys. Res.*, *102*(D10), 11,181–11,200, doi:10.1029/97JD00148.

Myhre, G., D. Shindell, F.-M. Bréon, W. Collins, J. Fuglestvedt, J. Huang, D. Koch, J.-F. Lamarque, D. Lee, B. Mendoza, T. Nakajima, A. Robock, G. Stephens, T. Takemura, and H. Zhang (2013), Anthropogenic and Natural Radiative Forcing, in *Climate Change 2013: The Physical Science Basis. Contribution of Working Group I to the Fifth Assess-*

ment Report of the Intergovernmental Panel on Climate Change, Cambridge University Press, Cambridge, United Kingdom and New York, NY, USA.

Phillpot, H. R., and J. W. Zillman (1970), The surface temperature inversion over the Antarctic Continent, *J. Geophys. Res.*, *75*(21), 4161–4169, doi: 10.1029/JC075i021p04161.

Pithan, F., and T. Mauritsen (2014), Arctic amplification dominated by temperature feedbacks in contemporary climate models, *Nature Geosci.*, *7*, 181–184, doi: 10.1038/ngeo2071.

Schmithüsen, H., J. Notholt, G. König-Langlo, P. Lemke, and T. Jung (2015), How increasing CO2 leads to an increased negative greenhouse effect in Antarctica, *Geophys. Res. Lett.*, *42*(23), 10,422–10,428, doi:10.1002/2015GL066749, 2015GL066749.

Sejas, S. A., M. Cai, G. Liu, P. C. Taylor, and K.-K. Tung (2016), A Lagrangian view of longwave radiative fluxes for understanding the direct heating response to a CO2 increase, *J. Geophys. Res. Atmos.*, *121*(11), 6191–6214, doi:10.1002/2015JD024738, 2015JD024738.

Serreze, M. C., R. C. Schnell, and J. D. Kahl (1992), Low-Level Temperature Inversions of the Eurasian Arctic and Comparisons with Soviet Drifting Station Data, *J Climate.*, *5*(6), 615–629, doi:10.1175/1520-0442(1992)005<0615:LLTIOT>2.0.CO;2.

Shell, K. M., J. T. Kiehl, and C. A. Shields (2008), Using the radiative kernel technique to calculate climate feedbacks in NCAR's Community Atmospheric Model, *J. Climate*, *21*, 2269–2282, doi:10.1175/2007JCLI2044.1.

Shine, K. P., and P. M. Forster (1999), The effect of human activity on radiative forcing of climate change: a review of recent developments, *Global and Planetary Change*, *20*(4), 205–225, doi:10.1016/S0921-8181(99)00017-X.

Soden, B. J., I. M. Held, R. Colman, K. M. Shell, J. T. Kiehl, and C. A. Shields (2008), Quantifying climate feedbacks using radiative kernels, *J. Climate*, *21*, 3504–3520, doi: 10.1175/2007JCI2110.1.

Stephens, G. L., M. Wild, P. W. S. Jr., T. L'Ecuyer, S. Kato, and D. S. Henderson (2012), The global character of the flux of downward longwave radiation, *J. Climate*, *25*(7), 2329–2340, doi:10.1175/JCLI-D-11-00262.1.

Stevenson, D. S., P. J. Young, V. Naik, J.-F. Lamarque, D. T. Shindell, A. Voulgarakis, R. B. Skeie, S. B. Dalsoren, G. Myhre, T. K. Berntsen, G. A. Folberth, S. T. Rumbold, W. J. Collins, I. A. MacKenzie, R. M. Doherty, G. Zeng, T. P. C. van Noije, A. Strunk,

D. Bergmann, P. Cameron-Smith, D. A. Plummer, S. A. Strode, L. Horowitz, Y. H. Lee, S. Szopa, K. Sudo, T. Nagashima, B. Josse, I. Cionni, M. Righi, V. Eyring, A. Conley, K. W. Bowman, O. Wild, and A. Archibald (2013), Tropospheric ozone changes, radiative forcing and attribution to emissions in the Atmospheric Chemistry and Climate Model Intercomparison Project (ACCMIP), *Atmos. Chem. Phys.*, *13*(6), 3063–3085, doi: 10.5194/acp-13-3063-2013.

Thomas, G. E., and K. Stamnes (1999), *Radiative Transfer in the Atmosphere and Ocean*, Cambridge Atmospheric and Space Science Series, Cambridge Univ. Press, Cambridge.

Thompson, S. L., V. Ramaswamy, and C. Covey (1987), Atmospheric effects of nuclear war aerosols in general circulation model simulations: Influence of smoke optical properties, *J. Geophys. Res. Atmos.*, *92*(D9), 10,942–10,960, doi:10.1029/JD092iD09p10942.

Turco, R. P., O. B. Toon, T. P. Ackerman, J. B. Pollack, and C. Sagan (1983), Nuclear winter: global consequences of multple nuclear explosions, *Science*, *222*(4630), 1283–1292.

Figure 1.

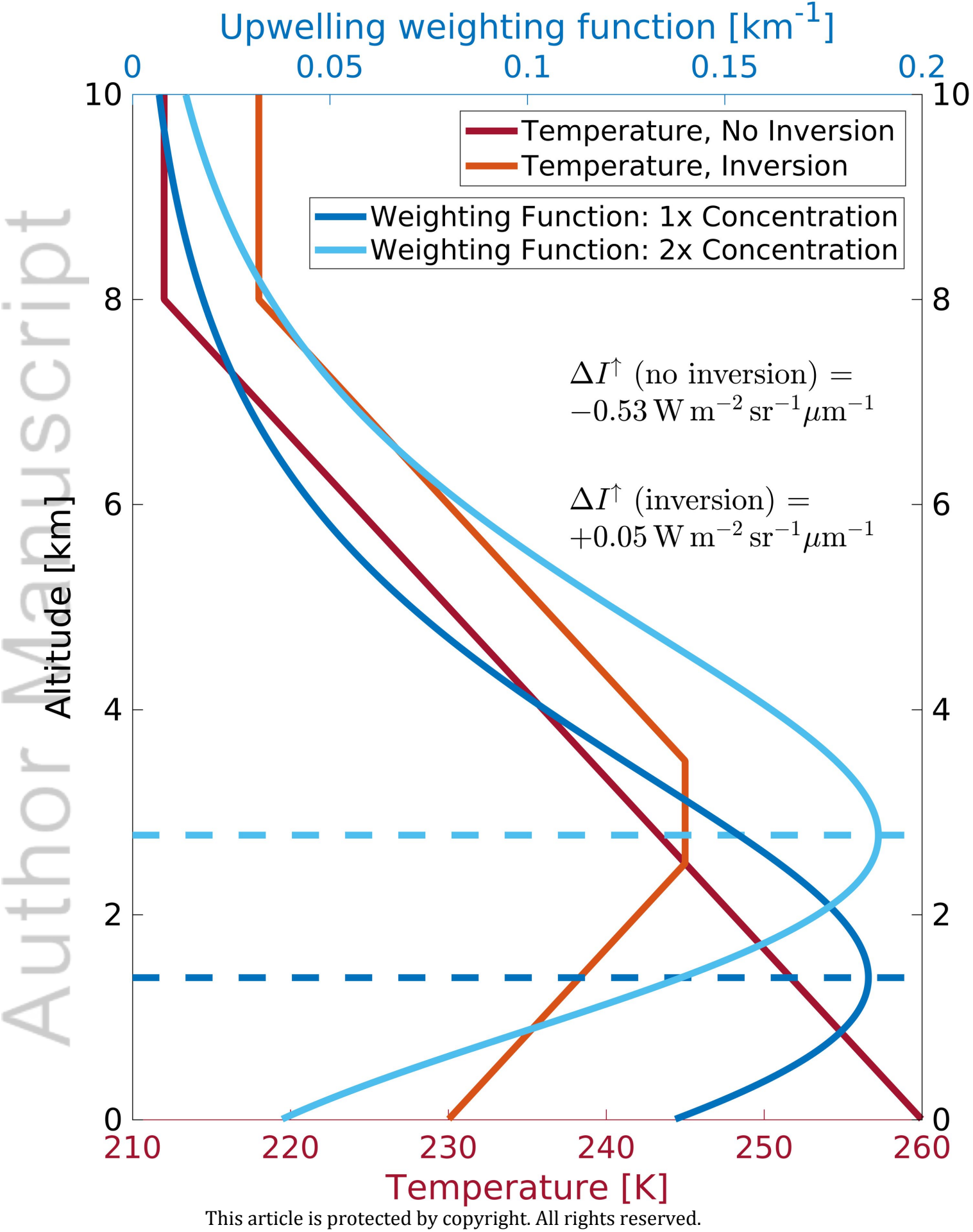

Figure 2.

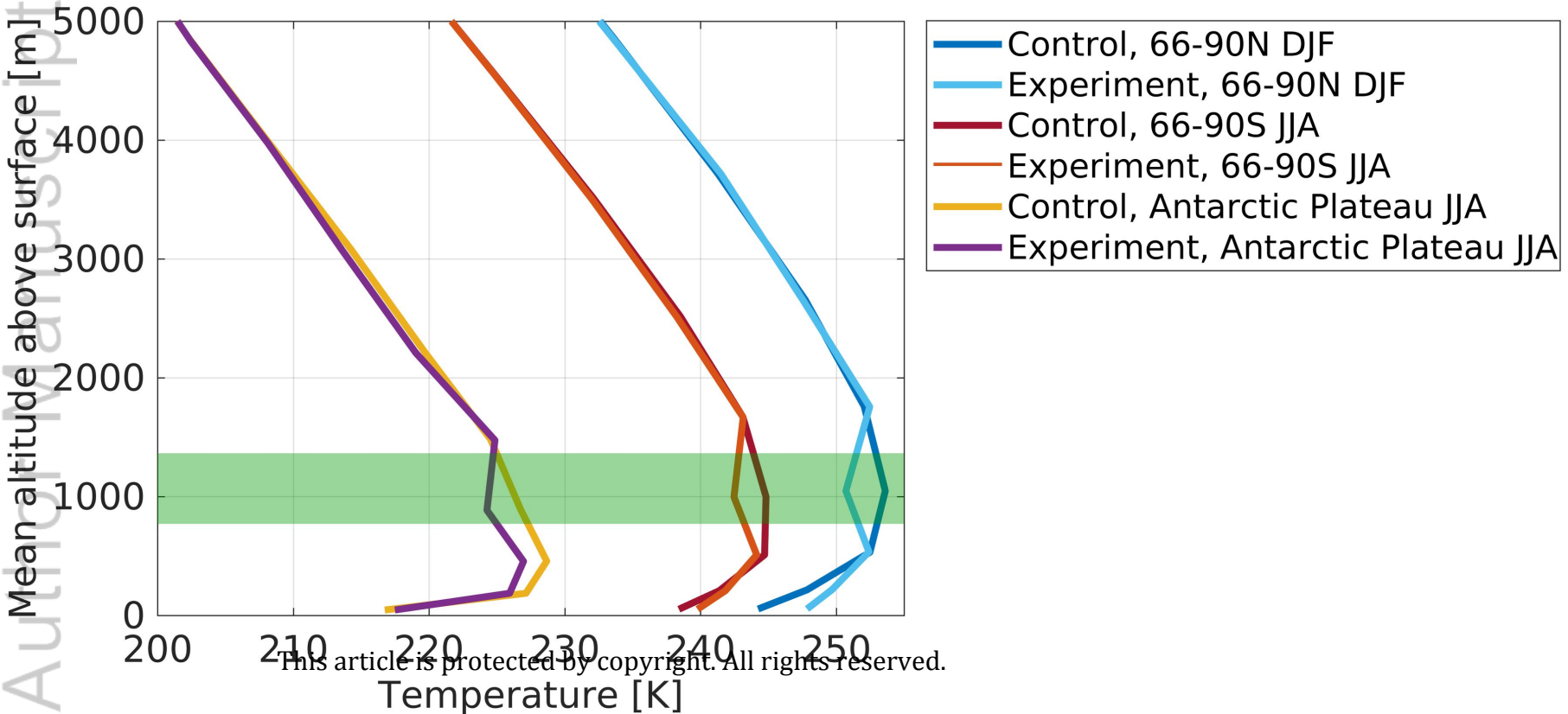

Figure 3.

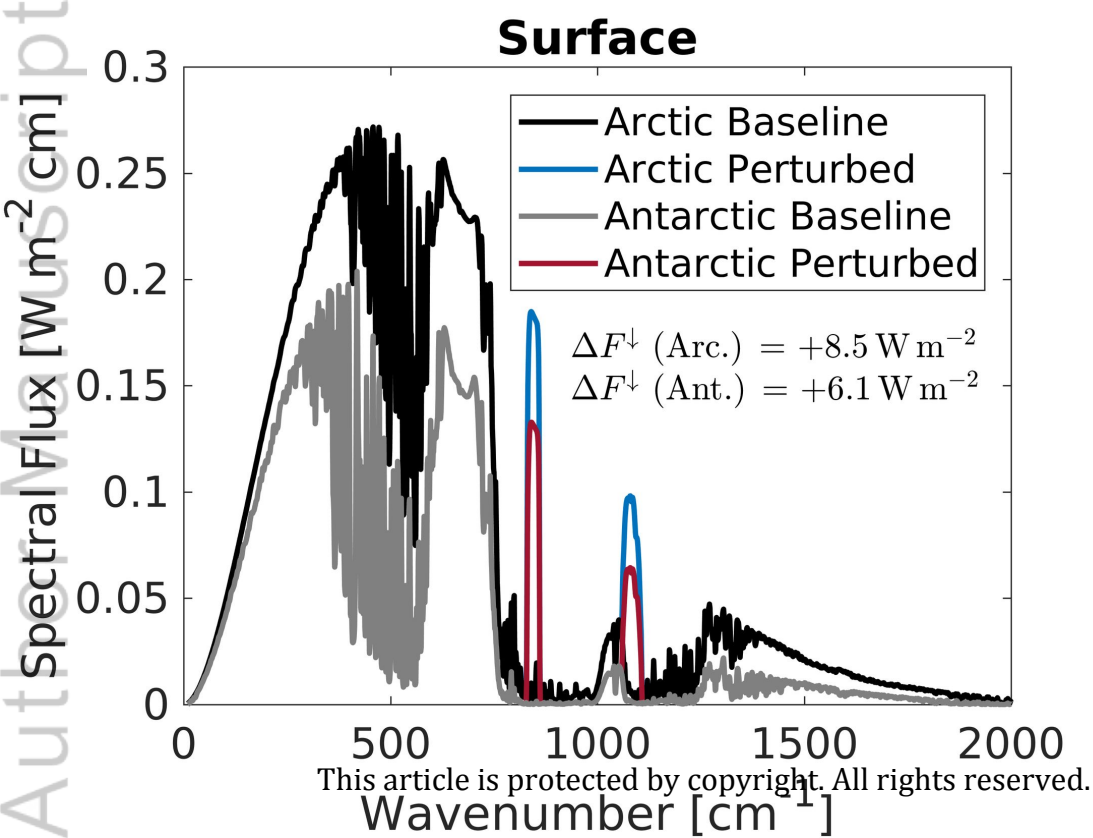

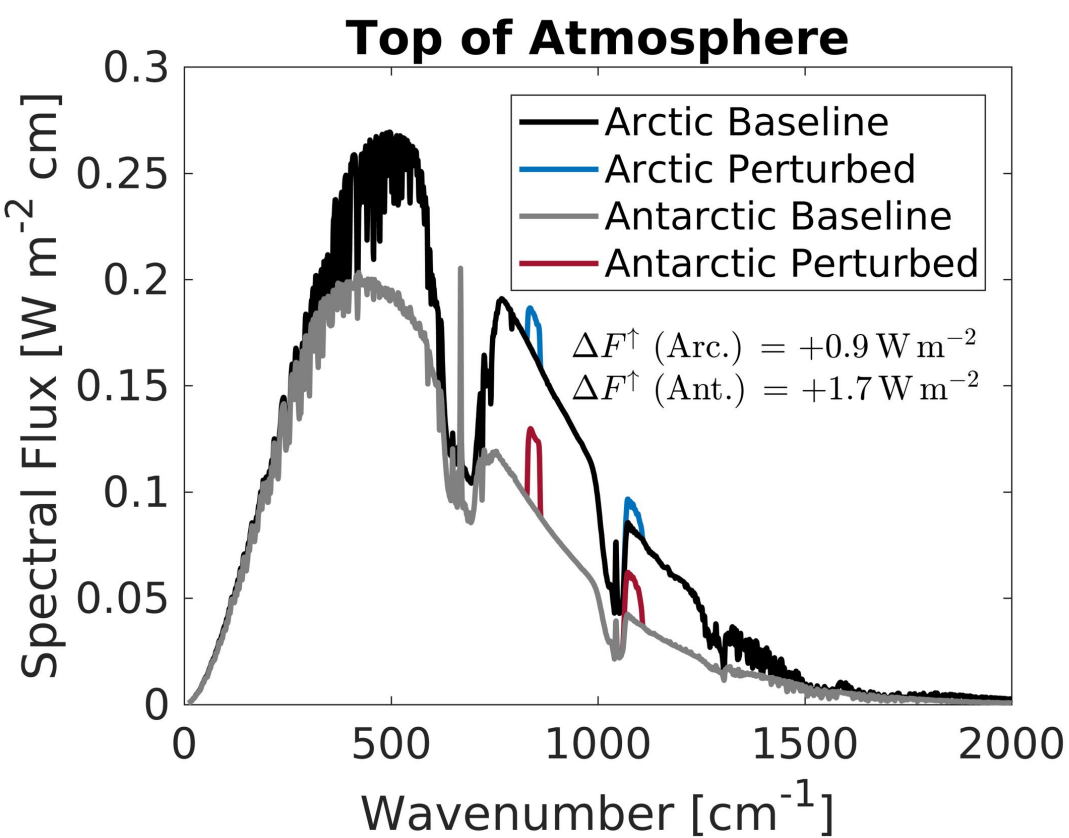

Figure 4.

Longwave Radiative Forcings

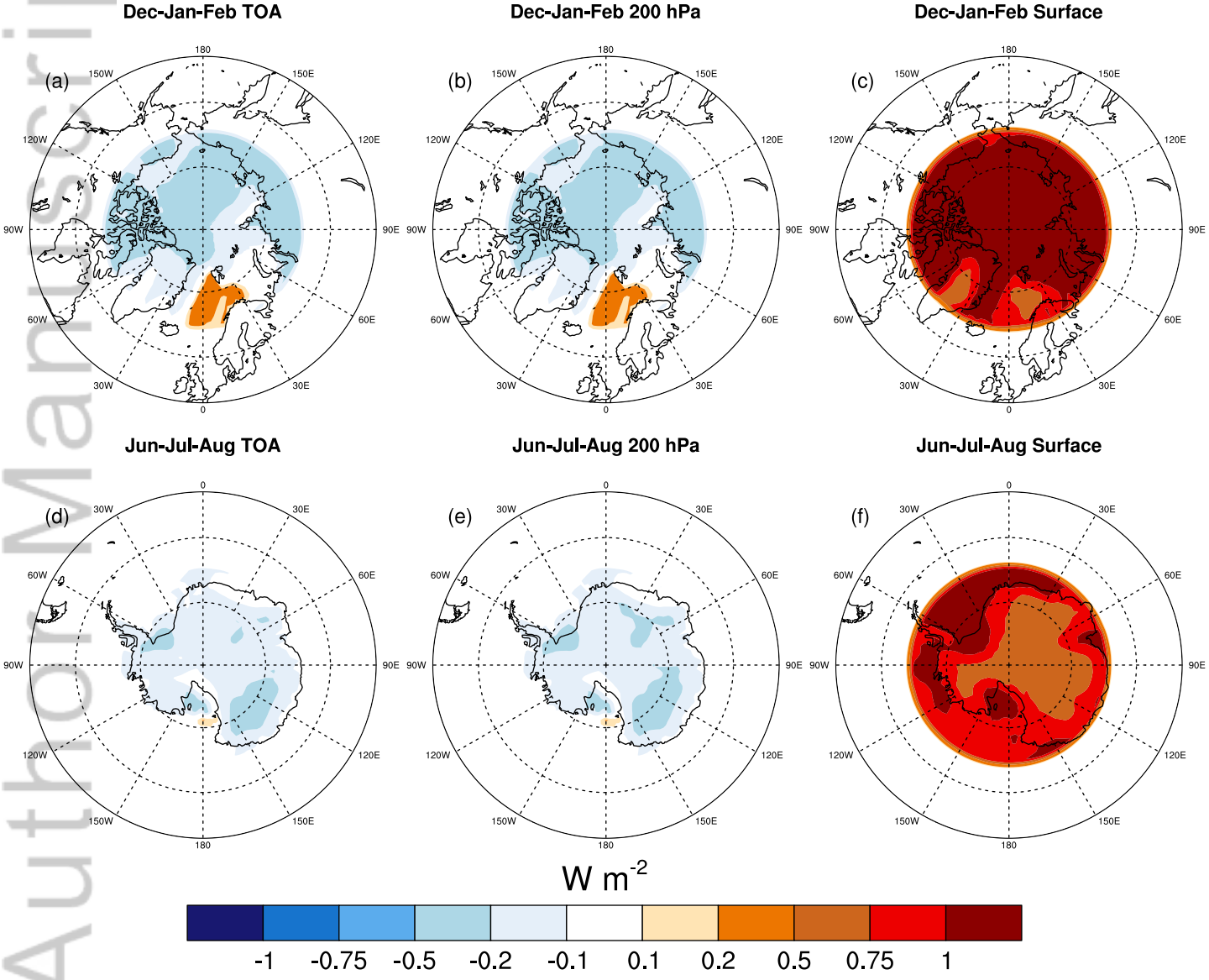

Figure 5.